IJMMM International Journal of Minerals, Metallurgy and Materials 矿物冶金与材料学报（英文版）

Metal-organic framework derived $NiFe_2O_4/FeNi_3@C$ composite for efficient electrocatalytic oxygen evolution reaction

Fangna Dai, Zhifei Wang, Huakai Xu, Chuanhai Jiang, Yuguo Ouyang, Chunyu Lu, Yuan Jing, Shiwei Yao, and Xiaofei Wei

Cite this article as:
Fangna Dai, Zhifei Wang, Huakai Xu, Chuanhai Jiang, Yuguo Ouyang, Chunyu Lu, Yuan Jing, Shiwei Yao, and Xiaofei Wei, Metal-organic framework derived $NiFe_2O_4/FeNi_3@C$ composite for efficient electrocatalytic oxygen evolution reaction, *Int. J. Miner. Metall. Mater.*, 30(2023), No. 10, pp. 1914-1921. https://doi.org/10.1007/s12613-023-2721-7

View the article online at SpringerLink or IJMMM Webpage.

Articles you may be interested in

Bao Liu, Shuo Wang, Cheng-yan Wang, Bao-zhong Ma, and Yong-qiang Chen, Electrochemical behavior and corrosion resistance of IrO_2–ZrO_2 binary oxide coatings for promoting oxygen evolution in sulfuric acid solution, *Int. J. Miner. Metall. Mater.*, 27(2020), No. 2, pp. 264-273. https://doi.org/10.1007/s12613-019-1847-0

Guo-qing Li, Pu-kang Wen, Chen-qiang Gao, Tian-yi Zhang, Jun-yang Hu, Yu-hao Zhang, Shi-you Guan, Qing-feng Li, and Bing Li, Effects of CeO_2 pre-calcined at different temperatures on the performance of Pt/CeO_2–C electrocatalyst for methanol oxidation reaction, *Int. J. Miner. Metall. Mater.*, 28(2021), No. 7, pp. 1224-1232. https://doi.org/10.1007/s12613-020-2076-2

Rui-qi Yang, Na Liang, Xuan-yu Chen, Long-wei Wang, Guo-xin Song, Yan-chen Ji, Na Ren, Ya-wei Lü, Jian Zhang, and Xin Yu, Sn/Sn_3O_{4-x} heterostructure rich in oxygen vacancies with enhanced visible light photocatalytic oxidation performance, *Int. J. Miner. Metall. Mater.*, 28(2021), No. 1, pp. 150-159. https://doi.org/10.1007/s12613-020-2131-z

Tao Wei, Zao-hong Zhang, Qi Zhang, Jia-hao Lu, Qi-ming Xiong, Feng-yue Wang, Xin-ping Zhou, Wen-jia Zhao, and Xiang-yun Qiu, Anion-immobilized solid composite electrolytes based on metal-organic frameworks and superacid ZrO_2 fillers for high-performance all solid-state lithium metal batteries, *Int. J. Miner. Metall. Mater.*, 28(2021), No. 10, pp. 1636-1646. https://doi.org/10.1007/s12613-021-2289-z

Fabiane Carvalho Ballotin, Mayra Nascimento, Sara Silveira Vieira, Alexandre Carvalho Bertoli, Ottávio Carmignano, Ana Paula de Carvalho Teixeira, and Rochel Montero Lago, Natural Mg silicates with different structures and morphologies: Reaction with K to produce K_2MgSiO_4 catalyst for biodiesel production, *Int. J. Miner. Metall. Mater.*, 27(2020), No. 1, pp. 46-54. https://doi.org/10.1007/s12613-019-1891-9

Ying Liu, Yong-an Zhang, Wei Wang, Dong-sheng Li, and Jun-yi Ma, Microstructure and electrolysis behavior of self-healing Cu-Ni-Fe composite inert anodes for aluminum electrowinning, *Int. J. Miner. Metall. Mater.*, 25(2018), No. 10, pp. 1208-1216. https://doi.org/10.1007/s12613-018-1673-9

IJMMM WeChat

QQ author group

International Journal of Minerals, Metallurgy and Materials
Volume 30, Number 10, October 2023, Page 1914
https://doi.org/10.1007/s12613-023-2721-7

Metal-organic framework derived $NiFe_2O_4/FeNi_3@C$ composite for efficient electrocatalytic oxygen evolution reaction

Fangna Dai, Zhifei Wang, Huakai Xu, Chuanhai Jiang, Yuguo Ouyang, Chunyu Lu, Yuan Jing, Shiwei Yao, and Xiaofei Wei✉

School of Materials Science and Engineering, China University of Petroleum, Qingdao 266580, China

(Received: 30 March 2023; revised: 3 August 2023; accepted: 9 August 2023)

Abstract: Reducing the cost and improving the electrocatalytic activity are the key to developing high efficiency electrocatalysts for oxygen evolution reaction (OER). Here, bimetallic NiFe-based metal-organic framework (MOF) was prepared by solvothermal method, and then used as precursor to prepare NiFe-based MOF-derived materials by pyrolysis. The effects of different metal ratios and pyrolysis temperatures on the sample structure and OER electrocatalytic performance were investigated and compared. The experimental results showed that when the metal molar ratio was Fe : Ni = 1:5 and the pyrolysis temperature was 450°C, the sample ($FeNi_5$-MOF-450) exhibits a composite structure of $NiFe_2O_4/FeNi_3/C$ and owns the superior electrocatalytic activity in OER. When the current density is 100 $mA\cdot cm^{-2}$, the overpotential of the sample was 377 mV with Tafel slope of 56.2 $mV\cdot dec^{-1}$, which indicates that $FeNi_5$-MOF-450 exhibits superior electrocatalytic performance than the commercial RuO_2. Moreover, the long-term stability of $FeNi_5$-MOF-450 further promotes its development in OER. This work demonstrated that the regulatory methods such as component optimization can effectively improve the OER catalytic performance of NiFe-based MOF-derived materials.

Keywords: metal-organic framework derivatives; NiFe-based electrocatalysts; electrocatalytic performance; oxygen evolution reaction

1. Introduction

The green and sustainable energy conversion and storage technology is the key to solve the problem of environmental pollution and energy shortage [1–3]. The technology of hydrogen production by water electrolysis and fuel cell is the optimal choice to realize the conversion between hydrogen energy and electric energy [4–5]. However, due to the complex proton–electron transfer process of oxygen evolution reaction (OER), OER has high overpotential and slow reaction kinetics, which seriously restricts the efficiency of hydrogen production and fuel cells by electrolytic water splitting [3,6–8]. Therefore, designing and synthesizing efficient OER catalysts to reduce OER reaction overpotential and accelerate the reaction rate is a focus of research. The best OER electrocatalysts reported so far are mainly noble metal-based catalysts, such as RuO_2 and IrO_2 [9–10]. However, low precious metal reserves in the earth's crust, high cost, and short service life of precious metal catalysts seriously restrict the large-scale commercial application in the field of hydrogen production by water electrolysis and fuel cells [11–12].

Fortunately, more and more studies have reported that transition metal-based materials (e.g., MnO_2, LDH, etc.) abundant in the crust exhibited good electrocatalytic OER properties [13–17]. Specially, NiFe-based catalysts showed high efficiency OER electrocatalysis. Over the past decade, NiFe-based oxides, hydroxides, sulfides, and selenides have been explored for OER reactions, showing great promise for NiFe-based materials as low-cost OER catalysts [18–21]. Among various NiFe-based OER catalysts, NiFe-based oxides are effective OER catalysts and have been shown to have great potential for OER electrocatalysis [22–23]. Moreover, spinel compounds with AB_2O_4 general form have attracted special attention due to their stable structure and abundant catalytic active sites, and become a very competitive OER electrocatalyst [24]. In addition, the abundant element valence and structural flexibility in its unique spinel configuration can provide more possibilities to improve its catalytic OER. For example, Chen *et al.* [25] synthesized a $NiFe_2O_4$ spinel electrocatalyst with 100% (111) face exposure directly on nickel foam (NF) by hydrothermal methods. Abundant vacancy defects were produced on the $NiFe_2O_4$ (111) surface by argon plasma etching. The experimental results showed that the introduction of multi-vacancy effectively regulated the electronic structure of the active center and optimized the adsorption energy of H_2O molecules and reaction intermediates on electrocatalysts, which was the key to reduce reaction kinetics and improve electrochemical OER activity. In addition to metal oxides, NiFe alloy materials also show excellent OER catalytic performance [26–29]. For ex-

---

✉ Corresponding author: Xiaofei Wei E-mail: b21140026@s.upc.edu.cn

ample, Xu *et al.* [26] found that different Ni/Fe ratios lead to significant differences in surface composition and structure of NiFe alloys, which modulated their electrocatalytic performance in OER. In addition, the ultra-thin oxide layer on the surface of NiFe alloys is the key to the high catalytic activity of NiFe alloys. The results of experimental characterization and theoretical calculation exhibited that Ni_4Fe_1 alloy with well-customized oxide/metal interface contributed to the formation of active substances, and the number of oxygen vacancies in the surface oxides optimized the adsorption interaction between O^* intermediate and Ni_4Fe_1 alloy, thus greatly improving its electrocatalytic activity.

Due to large surface area, abundant and uniformly dispersed active sites, adjustable chemical composition, and frame structure, metal-organic framework (MOF) materials are expected to replace noble metal-based catalysts as efficient OER pre-catalysts [30–33]. Li *et al.* [34] significantly improved the OER catalytic activity of MOF by introducing other metal cations into MIL-53(Fe). When $FeNi_{0.24}Co_{0.4}$-MIL-53 reached the current density of 20 $mA\cdot cm^{-2}$, only 236 mV of overpotential was required, and the Tafel slope was 52.2 $mV\cdot dec^{-1}$. In addition, Zhang *et al.* [35] prepared a series of bimetallic organic frameworks by a one-step method and obtained bimetallic oxides by pyrolysis of these bimetallic MOFs. These oxide catalysts showed good OER catalytic activity. The optimal catalyst needed only 335 mV overpotential to reach 10 $mA\cdot cm^{-2}$ current density in 1.0 M KOH, and the Tafel slope was 55.6 $mV\cdot dec^{-1}$.

Based on the above discussion, a series of MOF pyrolysis products in this work were prepared by high-temperature calcination using FeNi-MOF as precursor and their OER electrocatalytic performance was investigated. Compared with other samples, $NiFe_2O_4/FeNi_3/C$ material formed at 450°C ($FeNi_5$-MOF-450) exhibited the optimal OER activity, and the current densities of 10 and 100 $mA\cdot cm^{-2}$ can be reached at the overpotentials of 307 and 377 mV with the Tafel slope of 56.2 $mV\cdot dec^{-1}$. Moreover, $FeNi_5$-MOF-450 displayed the superior stability during the electrochemical tests. This work provides a feasible way to develop new and efficient transition metal based OER catalysts.

2. Experimental

2.1. Synthesis of $FeNi_n$-MOF (n = 0, 3, 5, and 7)

$FeNi_n$-MOF can be obtained by solvothermal reaction, where n represents the mole ratio of added Fe and Ni. In a typical synthesis of $FeNi_5$-MOF, 16.6 mg (0.1 mmol) of 1,4-terephthalic acid (H_2BDC), 145.4 mg (0.5 mmol) of nickel nitrate hexahydrate ($Ni(NO_3)_2\cdot 6H_2O$), and 27.0 mg (0.1 mmol) of ferric chloride hexahydrate ($FeCl_3\cdot 6H_2O$) were weighed and dissolved in 12 mL N,N-dimethylacetamide (DMA). The reaction solution was then transferred to a 20 mL high pressure reactor. The reactor was placed in the oven at 150°C for 6 h, and then cooled to room temperature. The product was washed three times each with water and ethanol, and dried in 60°C vacuum for 12 h. In addition, Fe-MOF, $FeNi_3$-MOF, and $FeNi_7$-MOF were synthesized as control groups. Among them, the synthesis steps of Fe-MOF, $FeNi_3$-MOF, and $FeNi_7$-MOF were exactly the same as those of $FeNi_5$-MOF ($FeNi_3$, $FeNi_5$, and $FeNi_7$ merely reflect the initial molar ratio of raw materials), except the addition amounts of $Ni(NO_3)_2\cdot 6H_2O$ were different (0, 0.3, and 0.7 mmol of $Ni(NO_3)_2\cdot 6H_2O$ were added, respectively).

2.2. Synthesis of $FeNi_n$-MOF-T

0.2 g $FeNi_5$-MOF sample prepared in the previous step was weighed into the porcelain boat and the porcelain boat was placed in the tubular furnace. The tubular furnace was heated to 450°C with the heating rate of 5$°C\cdot min^{-1}$ and kept for 1 h in nitrogen atmosphere. After naturally cooled to room temperature, $FeNi_n$-MOF-450 was obtained. In addition, samples such as $FeNi_n$-MOF-200, $FeNi_n$-MOF-300, $FeNi_n$-MOF-400, $FeNi_n$-MOF-500, $FeNi_n$-MOF-550, and $FeNi_n$-MOF-600 were synthesized as control groups. Except for changing the calcination temperature (T), the other steps are exactly the same as the synthesis steps of $FeNi_n$-MOF-450.

2.3. Material characterization

The phase of electrocatalysts was characterized through X-ray diffraction (XRD, Bruker D2 PHASER). The morphologies were obtained using a scanning electron microscope (SEM, HITACHI S-4800) and a transmission electron microscope (TEM, China JEM-1400Plus). Fourier transform infrared (FT-IR) spectra were recorded by Bruker VERTEX70. Raman spectra were obtained by a LabRAM HR confocal Raman microscopy system. X-ray photoelectron spectroscopy (XPS) spectra were recorded using a Thermo Scientific ESCALAB 250Xi.

2.4. Electrochemical measurements

All OER tests in this article were performed with a typical three-electrode system (Gamry INTERFACE 1000 T) at room temperature. The synthetic samples, a graphite rod, and a calomel electrode (SCE) were separately used as the working electrode, the counter electrode, and the reference electrode. The test solution was 1.0 M KOH solution. All test results were corrected by the formula ($E_{RHE} = E_{SCE} + 0.0592pH + 0.242$, where E_{RHE} is the reversible hydrogen electrode potential after conversion, and E_{SCE} is the actual measured potential using saturated calomel electrode.) and corrected for the iR-drop. Before the OER test, the working electrode was scanned with cyclic voltammetry (CV) until the sample was stable. Linear sweep voltammetry (LSV) were recorded at 5 $mV\cdot s^{-1}$. Electrochemical impedance spectroscopy (EIS) measurements were performed in the frequency range of 10^{-5} to 10^{-2} Hz with the amplitude of 5 mV. To obtain the electrochemical double layer capacitance (C_{dl}) value, CV curves were collected at 1.38 to 1.48 V (vs. reversible hydrogen electrode (RHE)) with the scan rates of 20 to 100 $mV\cdot s^{-1}$, respectively. The C_{dl} values can be calculated by using the linear slopes of curves of $\Delta j/2$ vs. scan rate (Δj stands for the difference in current density). The electrochemical active area (ECSA) and the normalized current density were calculated using the double layer capacitance, according to the equations ECSA $=C_{\mathrm{dl}}/C_{\mathrm{s}}$ and $j_{\mathrm{normalized}} = j/\mathrm{ECSA}$, where C_{s} is the specific capacitance of the material and j is current density. Tafel plots were calculated to understand the reaction mechanism of OER performance according to the Tafel equation $\eta = b \times \lg j + a$ (η stands for overpotential, j stands for current density, and b stands for slope). The stability was evaluated by using CV at 100 $\mathrm{mV \cdot s^{-1}}$ for 2000 cycles. The long-term stability test was completed using chronopotentiometric measurement without iR drop compensation.

3. Results and discussion

3.1. Material morphology and structure characterization

The preparation process of FeNi$_n$-MOF-T catalyst is shown in Fig. 1. Firstly, $\mathrm{FeCl_3 \cdot 6H_2O}$ and $\mathrm{Ni(NO_3)_2 \cdot 6H_2O}$ were used as nickel and iron sources, respectively. $\mathrm{H_2BDC}$ and DMA were severed as organic ligand and solvent. The product (FeNi$_n$-MOF) can be obtained by solvothermal reaction at 150°C for 6 h. Then, FeNi$_n$-MOF was used as the precursor and further calcined at different temperatures for 1 h, and the calcined products (FeNi$_n$-MOF-T) were obtained.

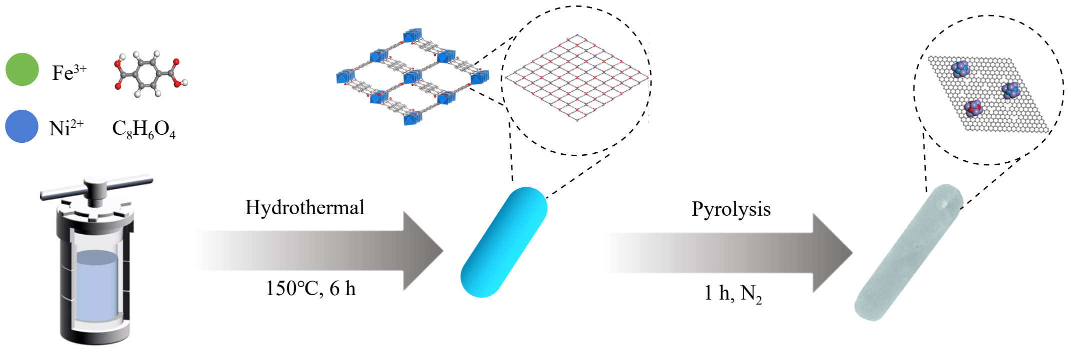

Fig. 1. Schematic illustration of the synthesis of FeNi$_n$-MOF-T.

According to previous reports [36], FeNi$_n$-MOF was synthesized by solvothermal method in this work. In order to investigate the material structure change of FeNi$_5$-MOF during the pyrolysis process, the structural information of MOF and the products formed by the calcination of MOF at different temperatures (FeNi$_5$-MOF-T, T = 200, 300, 400, 450, 500, 550, and 600°C) were deteced by XRD and thermogravimetric analysis (TGA). As shown in Fig. 2(a), the diffraction peak of FeNi$_5$-MOF sample corresponded well with that of MIL-53 (Fe), indicating the successful preparation of the precursor of MOF. However, due to some lattice expansion caused by the incorporation of Ni in the process of MOF synthesis, the FeNi$_5$-MOF diffraction peak shifted to the left [37]. The diffraction peaks of FeNi$_5$-MOF-450 corresponded to $\mathrm{NiFe_2O_4}$ (PDF#54-0964) and $\mathrm{FeNi_3}$ (PDF#38-0419), indicating that $\mathrm{NiFe_2O_4}$ and $\mathrm{FeNi_3}$ nanoparticles were produced by MOF pyrolysis at 450°C. Yet, the XRD data of FeNi$_5$-MOF-500 and FeNi$_5$-MOF-600 showed that the diffraction peak corresponding to $\mathrm{NiFe_2O_4}$ was weakened and the intensity corresponding to $\mathrm{FeNi_3}$ was enhanced, which indicated that the metal oxides gradually disappeared and Fe and Ni formed alloy nanoparticles with the pyrolysis temperature rising. Furtherly, this was also verified by the TGA (Fig. S1).

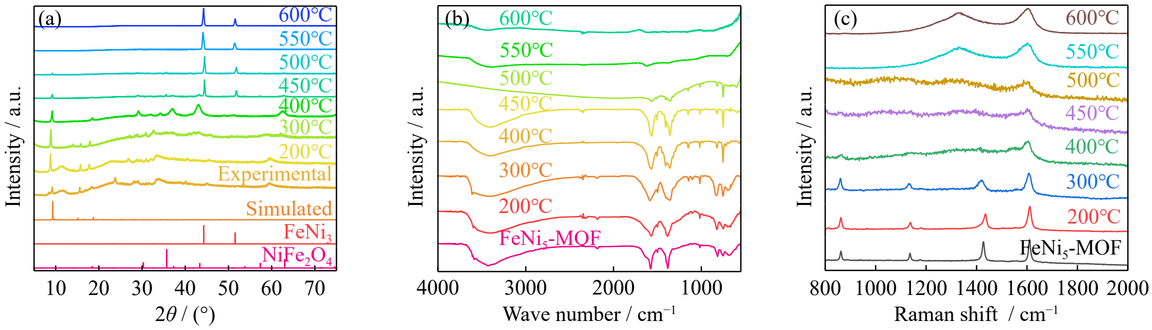

Fig. 2. (a) XRD patterns of FeNi$_5$-MOF and products at different temperatures; (b) FT-IR spectra and (c) Raman spectra of FeNi$_5$-MOF products calcined at different temperatures.

In addition, in order to analyze the structural changes of materials during heat treatment, the functional groups of products calcined at different temperatures were characterized by FT-IR spectra. As shown in Fig. 2(b) and Table 1, the absorption peak of FeNi$_5$-MOF at 3634 $\mathrm{cm^{-1}}$ indicated the presence of physically adsorbed water molecules in the MOF channel. When the calcination temperature exceeded 300°C, the absorption peak here disappeared. The absorption peaks near 3420 and 1580 $\mathrm{cm^{-1}}$ respectively represented the absorption peaks corresponding to different vibration modes of

Table 1. FT-IR spectra peak positions of $FeNi_5$-MOF and $FeNi_5$-MOF-*T* (*T* = 200, 300, 400, 450, 500, 550, and 600°C; *ν* stands for wavenumber)

Material	$\nu(H_2O)$ / cm^{-1}	ν(–OH) / cm^{-1}	ν(benzene) / cm^{-1}	ν(C–O) / cm^{-1}	ν(phenyl-binomial substitution) / cm^{-1}
$FeNi_5$-MOF	3634	3425, 1586	1500	2185	753, 820
$FeNi_5$-MOF-200	3634	3418, 1571	1500	2181	748, 824
$FeNi_5$-MOF-300	3640	3422, 1589	1500	2188	754, 827
$FeNi_5$-MOF-400	—	3421, 1571	1504	—	752, 822
$FeNi_5$-MOF-450	—	3411, 1570	1505	—	752, 822
$FeNi_5$-MOF-500	—	—	1506	—	752, 822
$FeNi_5$-MOF-550	—	—	—	—	—
$FeNi_5$-MOF-600	—	—	—	—	—

the –OH group. When the calcination temperature was higher than 450°C, the absorption peaks of –OH group disappeared, indicating that there were still associated –OH groups in $FeNi_5$-MOF-450. This may be the presence of –COOH groups without coordination in $FeNi_5$-MOF. The absorption peak at 1500 cm^{-1} represented the absorption peak of benzene ring skeleton. This absorption peak did not disappear until the calcination temperature exceeded 500°C, which indicated that the MOF skeleton completely collapsed above 500°C. The absorption peaks near 750 and 820 cm^{-1} represented the p-binary substitution of benzene ring, and these two absorption peaks also disappeared when the calcination temperature exceeded 500°C, which also proved that the MOF skeleton completely collapsed when calcined above 500°C. The absorption peak near 2183 cm^{-1} was generated by the vibration of C–O bond. When the calcination temperature was higher than 300°C, the absorption peak near 2183 cm^{-1} disappeared, representing C–O bonds were broken. Combined with XRD pattern analysis, $NiFe_2O_4$ was formed inside the material when the temperature exceeded 300°C. The formation of spinel oxide (AB_2O_4) was confirmed by the absorption peaks in the range of 400–600 cm^{-1} in the infrared spectra of the materials calcined at 300–500°C.

In order to further explore the evolution process of MOF skeleton during pyrolysis, Raman spectroscopy was performed on $FeNi_5$-MOF and $FeNi_5$-MOF-*T* products at different temperatures, and the results were shown in Fig. 2(c). When the heat treatment temperature was lower than 300°C, the characteristic peaks of Raman did not change, which indicated that the material still maintained a complete frame structure. When the pyrolysis temperature reached more than 400°C, the Raman characteristic peaks at 860, 1134, and 1426 cm^{-1} disappeared, indicating the disintegration of the MOF skeleton. Moreover, D bands (1350 cm^{-1}) and G bands (1600 cm^{-1}) of carbon structure appeared in the Raman curves of $FeNi_5$-MOF-550 and $FeNi_5$-MOF-600, which demonstrated that the material was obviously carbonized when the heat treatment temperature exceeded 550°C.

Based on the above analysis, the morphologies of $FeNi_5$-MOF and $FeNi_5$-MOF-450 were investigated by SEM and TEM. As shown in Fig. 3(a), the morphology of $FeNi_5$-MOF showed a 1D rod-like appearance, which is similar to the classic MIL-53(Fe). This result was consistent with the XRD conclusion, further indicating that $FeNi_5$-MOF and MIL-53(Fe) have similar microscopic characteristics. The morphology of $FeNi_5$-MOF-450 (Fig. 3(b)) maintained the rod-like structure of the MOF, however after pyrolysis, the surface of the material was uneven and attached with a layer of

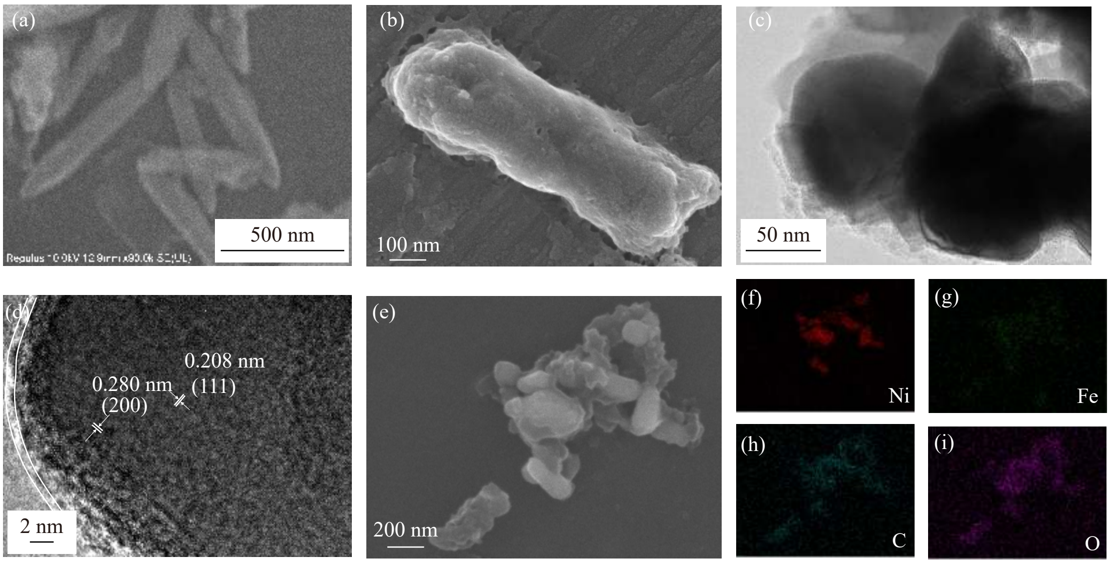

Fig. 3. (a) SEM image of $FeNi_5$-MOF; (b) SEM image of $FeNi_5$-MOF-450; (c) TEM and (d) HR-TEM images of $FeNi_5$-MOF-450; (e–i) elemental mapping images of $FeNi_5$-MOF-450.

carbon matrix, which is conducive to the charge transfer between the electrolyte and the active substances inside the catalyst, and improves the electrocatalytic activity of the sample [38]. At the same time, the outer carbon helped to protect active sites of the inner layer from the corrosion of the electrolyte. TEM images of $FeNi_5$-MOF-450 (Fig. 3(c)) showed that the diameter of nanoparticles inside the catalyst was about 80 nm. High-resolution transmission electron microscope (HR-TEM) images (Fig. 3(d)) showed that the crystal plane spacing was 0.208 and 0.280 nm, corresponding to the (111) facets of $NiFe_2O_4$ and the (200) facets of $FeNi_3$, and the particles were surrounded by carbon layer [39]. The elemental mapping images of $FeNi_5$-MOF-450 (Fig. 3(e)–(i)) showed that Ni, Fe, C, and O elements were evenly distributed in $FeNi_5$-MOF-450.

In order to investigate the chemical bonds and morphology of $FeNi_5$-MOF-450 surface atoms, XPS characterization analysis was performed on $FeNi_5$-MOF and $FeNi_5$-MOF-450. The XPS spectra of $FeNi_5$-MOF and $FeNi_5$-MOF-450 are shown in Fig. 4. Firstly, the characteristic peaks of Ni 2p, Fe 2p, C 1s, O 1s in Fig. 4(a) and (b) indicated the composition of elements in $FeNi_5$-MOF and $FeNi_5$-MOF-450, which was consistent with the result of elemental mapping. The Ni 2p spectrum of $FeNi_5$-MOF-450 can be fitted to six characteristic peaks, as shown in Fig. 4(c). Two characteristic peaks exist at 857.4 and 875.1 eV, corresponding to Ni^{2+} $2p_{3/2}$ and Ni^{2+} $2p_{1/2}$, respectively, which are attributed to the Ni–O bond. The peaks at 866.4 and 881.9 eV are satellite peaks. Compared with the Ni 2p diagram of $FeNi_5$-MOF, the Ni 2p characteristic peak of $FeNi_5$-MOF-450 moves 1.3 eV towards the direction of high binding energy, indicating that there is a strong electronic interaction between Ni and Fe after pyrolysis, which can regulate the electronic environment of the metal active center and thus improve the electrocatalytic performance. The Fe 2p spectrum of $FeNi_5$-MOF-450 can be fitted into 6 characteristic peaks, as shown in Fig. 4(d). The two characteristic peaks of 706.9 and 720.8 eV correspond to Fe $2p_{3/2}$ and Fe $2p_{1/2}$ of Fe^0. The two characteristic peaks of 711.4 and 725.6 eV correspond to Fe $2p_{3/2}$ and Fe $2p_{1/2}$ of Fe^{3+}, respectively, which attributed to the Fe–O bond. The peaks at 715.6 and 730.86 eV are two satellite peaks [40]. For the C 1s spectrum (Fig. 4(e)), 284.8, 286.7, and 288.4 eV are consistent with the binding energies of C=C, C=O, and O–C=O, respectively [41]. Compared with $FeNi_5$-MOF, the peak areas of the characteristic peaks C=O and O–C=O in $FeNi_5$-MOF-450 are obviously reduced, indicating the disintegration of the MOF skeleton. The O 1s spectrum (Fig. 4(f)) shows the presence of characteristic peaks of metal–oxygen (531.2 eV), C–O (532.9 eV), O–C=O (534.6 eV). Compared with $FeNi_5$-MOF, the M–O bond characteristic peaks in $FeNi_5$-MOF-450 are significantly decreased, which indicates the formation of alloy material in the material. These results further prove the formation of bimetallic oxides and bimetallic alloys.

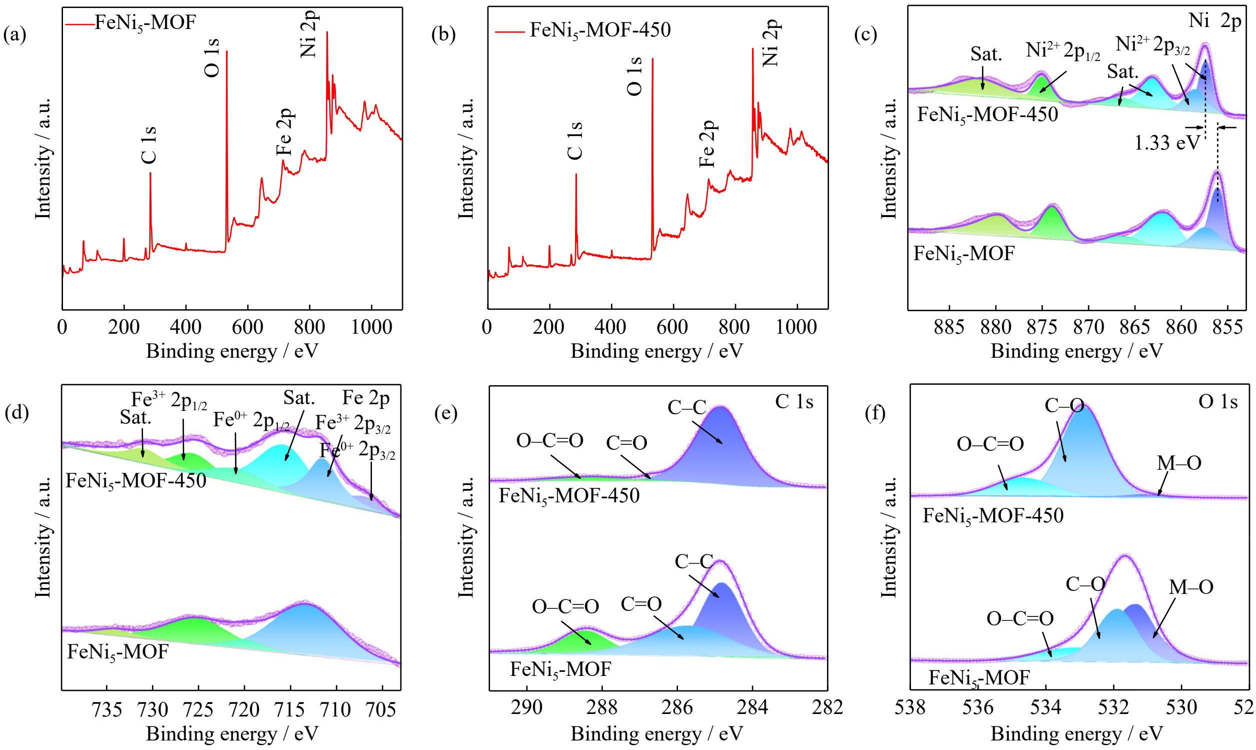

Fig. 4. (a) XPS full spectrum of $FeNi_5$-MOF; (b) XPS full spectrum of $FeNi_5$-MOF-450; (c) Ni 2p, (d) Fe 2p, (e) C 1s, and (f) O 1s spectrum.

3.2. Evaluation of OER electrocatalytic activity

OER electrocatalytic activity of all samples was tested in 1.0 M KOH. By comparing the OER activity of MOF precursors with Ni metal different amounts, it was proved that $FeNi_5$-MOF had the highest electrocatalytic activity (Fig. S2). In addition, RuO_2 was used as a comparison sample to conduct relevant OER activity tests to compare whether

$FeNi_5$-MOF-450 electrocatalyst has higher activity under the same test conditions. As shown in Fig. 5(a), although RuO_2 requires a lower overpotential than $FeNi_5$-MOF-450 at low current density (less than 44 $mA \cdot cm^{-2}$), $FeNi_5$-MOF-450 requires a lower overpotential to achieve higher current density beyond 44 $mA \cdot cm^{-2}$. As shown in Fig. 5(b), the overpotential of $FeNi_5$-MOF-450 at 10 $mA \cdot cm^{-2}$ (η_{10}) and 100 $mA \cdot cm^{-2}$ (η_{100}) are 307 mV and 377 mV, respectively, which are significantly lower than those of $FeNi_5$-MOF (325 mV and 401 mV), $FeNi_5$-MOF-400 (340 mV and 430 mV), and $FeNi_5$-MOF-600 (360 mV and 510 mV). As shown in Table 2, the electrocatalytic activity of $FeNi_5$-MOF-450 is also significantly better than those of other reported MOF-based or FeNi-based materials [35,42–52]. Therefore, $FeNi_5$-MOF-450 can be served as a promising electrocatalyst for OER. Fig. 5(c) shows the Tafel slope of $FeNi_5$-MOF and pyrolysis products at different temperatures. Similarly, The Tafel slope of $FeNi_5$-MOF-450 (56.2 $mV \cdot dec^{-1}$) is also significantly lower than those of $FeNi_5$-MOF (77.9 $mV \cdot dec^{-1}$), $FeNi_5$-MOF-400 (78.2 $mV \cdot dec^{-1}$), and $FeNi_5$-MOF-600 (99.4 $mV \cdot dec^{-1}$), which indicates that $FeNi_5$-MOF-450 has faster reaction kinetics than other catalysts in OER process.

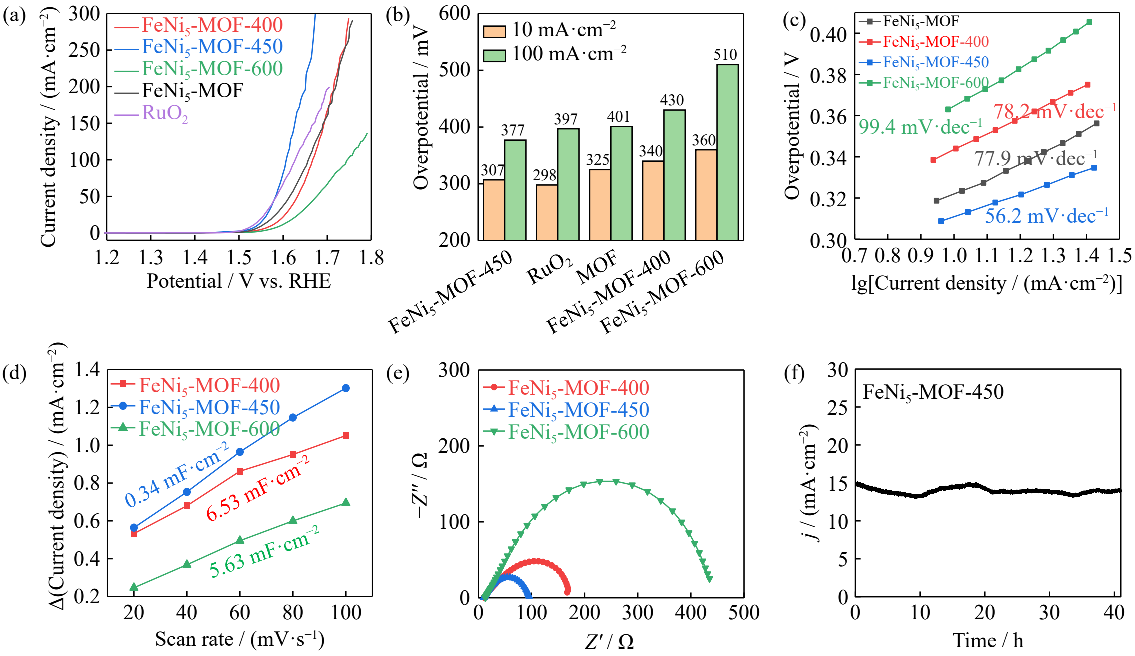

Fig. 5. (a) Polarization curve of different catalysts; (b) comparison diagram of overpotentials of different catalysts at current densities of 10 and 100 $mA \cdot cm^{-2}$; (c) Tafel slope of different catalysts; (d) Δj–scan rate diagram of different catalysts; (e) Nyquist diagram of different catalysts; (f) long-term stability testing of $FeNi_5$-MOF-450.

Table 2. Comparison of OER catalytic performance of $FeNi_5$-MOF-500 and other reported MOF-based or NiFe-based catalyst in the 1.0 M KOH (η_{10} and η_{100} refer to the overpotentials of catalysts at current densities of 10 and 100 $mA \cdot cm^{-2}$)

Catalysts	Overpotential / mV	Reference
$FeNi_5$-MOF-500	307 (η_{10}), 377 (η_{100})	This work
$CoNi_1@C$	355 (η_{10})	[35]
$Co_2P/CoP@NPGC$	340 (η_{10})	[42]
Ni@Ni-NC	371 (η_{10})	[43]
$Fe_{0.5}Ni_{0.5}Pc$-CP	317 (η_{10})	[44]
CoMo-MI-600	316 (η_{10})	[45]
$C@NiCo_{12}$	330 (η_{10})	[46]
Ni/NC-600	336 (η_{10})	[47]
$Ni(OH)_2@CoB$	320 (η_{10})	[48]
Ni_2MoN/NF	392.49 (η_{100})	[49]
Ni-OH/P	490 (η_{100})	[50]
Ni_9S_8	420 (η_{100})	[51]
Ni_7Fe_3	388 (η_{100})	[52]

To analyze the activity of $FeNi_5$-MOF-450 electrocatalysts, the ECSA values of $FeNi_5$-MOF-400, $FeNi_5$-MOF-450, and $FeNi_5$-MOF-600 were evaluated and compared. Since the ECSA of a catalyst is proportional to its double-layer capacitance (C_{dl}), the ECSA of a catalyst can be evaluated by measuring the double layer capacitance of the catalyst. Fig. S3 shows the CV curves of $FeNi_5$-MOF-400, $FeNi_5$-MOF-450, and $FeNi_5$-MOF-600 at different sweep speeds. C_{dl} data are shown in Fig. 5(d). The C_{dl} value of $FeNi_5$-MOF-450 is 9.34 $mF \cdot cm^{-2}$, which is significantly larger than those of $FeNi_5$-MOF-400 (6.53 $mF \cdot cm^{-2}$) and $FeNi_5$-MOF-600 (5.63 $mF \cdot cm^{-2}$). The moderate pyrolysis temperature (450°C) plays an important role in regulating the morphology and structure of catalyst, which increases the ECSA. Moreover, the suitable pyrolysis temperature adjusts the composition ratio between $NiFe_2O_4$ and $FeNi_3$, which is helpful for the formation of bimetallic alloys. The interface interaction between $NiFe_2O_4$ and $FeNi_3$ may improve the electronic structure of active sites in $FeNi_5$-MOF-450. Therefore, $FeNi_5$-MOF-450 exhibits the superior electrochemical activity than $FeNi_5$-MOF-400 and $FeNi_5$-MOF-600. In order to further investigate the catalytic kinetics of the catalyst, the EIS of $FeNi_5$-MOF-450 and other samples were tested. As shown in Fig. 5(e), the charge transfer resistance (R_{ct}) value of $FeNi_5$-MOF-450 is obviously lower than those of $FeNi_5$-MOF-400 and $FeNi_5$-MOF-600, indicating that the surface charge transfer rate of $FeNi_5$-MOF-450 electrocatalyst is faster. The stability of catalyst is also an important index to measure the performance of catalyst, which determines whether the catalyst can be used commercially on a large scale. Fig. 5(f) displayed that the stability of $FeNi_5$-MOF-450 was tested by constant voltage method. The $FeNi_5$-MOF-450 catalyst can work stably for more than 40 h at a voltage of 320 mV. TEM images and HR-TEM images of $FeNi_5$-MOF-450 after stability test further demonstrate that $FeNi_5$-MOF-450 can still maintain good structural stability after working more than 40 h (Fig. S4). Therefore, the above OER test results demonstrate that $FeNi_5$-MOF-450 is an OER electrocatalyst with great electrocatalytic performance.

4. Conclusion

In this work, $NiFe_2O_4/FeNi_3/C$ composites were prepared by solvothermal and high temperature pyrolysis. During the pyrolysis process, it is found that metal oxides are formed inside the material first, and when the temperature reaches a certain degree, FeNi alloy is formed inside the material and the metal oxides gradually disappear. Thanks to the synergistic effect between Ni and Fe metals and the interface interaction between $NiFe_2O_4$ and $FeNi_3$, the catalyst exhibits high efficiency OER electrocatalytic activity. The catalytic performance of the composite can be optimized by adjusting the metal molar ratio of Fe and Ni and the calcination temperature. Among them, the $FeNi_5$-MOF-450 electrocatalyst with the optimal performance showed better OER catalytic activity than commercial RuO_2 at high current density. Moreover, $FeNi_5$-MOF-450 owned a low overpotential of 377 mV at the current density of 100 $mA\cdot cm^{-2}$ with Tafel slope of 56.2 $mV\cdot dec^{-1}$, which was lower than that of commercial RuO_2 electrocatalyst. At the same time, the OER activity of $FeNi_5$-MOF-450 remained almost unchanged during the 40 h stability test. Therefore, $FeNi_5$-MOF-450 can perform as an efficient electrocatalyst for water splitting. This work provides a new way to prepare NiFe-based electrocatalysts with high catalytic performance of OER.

Acknowledgements

This work was supported by the Shandong Natural Science Fund (No. ZR2020KB010) and the Fundamental Research Funds for the Central Universities (No. 22CX 07010A).

Conflict of Interest

The authors declare that they have no conflicts of interest in this work.

Supplementary Information

The online version contains supplementary material available at https://doi.org/10.1007/s12613-023-2721-7.

References

[1] L. Zhang, C.J. Lu, F. Ye, *et al.*, Selenic acid etching assisted vacancy engineering for designing highly active electrocatalysts toward the oxygen evolution reaction, *Adv. Mater.*, 33(2021), No. 14, art. No. 2007523.

[2] I.S. Amiinu, Z.H. Pu, X.B. Liu, *et al.*, Multifunctional Mo–N/C@MoS_2 electrocatalysts for HER, OER, ORR, and Zn-air batteries, *Adv. Funct. Mater.*, 27(2017), No. 44, art. No. 1702300.

[3] N. Yao, G.W. Wang, H.N. Jia, *et al.*, Intermolecular energy gap-induced formation of high-valent cobalt species in CoOOH surface layer on cobalt sulfides for efficient water oxidation, *Angew. Chem. Int. Ed.*, 61(2022), No. 28, art. No. e202117178.

[4] Y.Q. Wang, S. Tao, H. Lin, *et al.*, Atomically targeting NiFe LDH to create multivacancies for OER catalysis with a small organic anchor, *Nano Energy*, 81(2021), art. No. 105606.

[5] K.Y. Zhu, X.F. Zhu, and W.S. Yang, Application of *in situ* techniques for the characterization of NiFe-based oxygen evolution reaction (OER) electrocatalysts, *Angew. Chem. Int. Ed.*, 58(2019), No. 5, p. 1252.

[6] K.X. Zhang and R.Q. Zou, Advanced transition metal-based OER electrocatalysts: Current status, opportunities, and challenges, *Small*, 17(2021), No. 37, art. No. 2100129.

[7] W.B. Chen, C.S. Wang, S.B. Su, H. Wang, and D.D. Cai, Synthesis of ZIF-9(III)/Co LDH layered composite from ZIF-9(I) based on controllable phase transition for enhanced electrocatalytic oxygen evolution reaction, *Chem. Eng. J.*, 414(2021), art. No. 128784.

[8] S. Yuan, J.Y. Peng, B. Cai, *et al.*, Tunable metal hydroxide-organic frameworks for catalysing oxygen evolution, *Nat. Mater.*, 21(2022), No. 6, p. 673.

[9] I.C. Man, H.Y. Su, F. Calle-Vallejo, *et al.*, Universality in oxygen evolution electrocatalysis on oxide surfaces, *ChemCatChem*, 3(2011), No. 7, p. 1159.

[10] C.L. Ma, W. Sun, W.Q. Zaman, *et al.*, Lanthanides regulated the amorphization–crystallization of IrO_2 for outstanding OER performance, *ACS Appl. Mater. Interfaces*, 12(2020), No. 31, p. 34980.

[11] F.Q. Zheng, W.F. Zhang, X.X. Zhang, Y.L. Zhang, and W. Chen, Sub-2 nm ultrathin and robust 2D FeNi layered double hydroxide nanosheets packed with 1D FeNi-MOFs for enhanced oxygen evolution electrocatalysis, *Adv. Funct. Mater.*, 31(2021), No. 43, art. No. 2103318.

[12] W.D. Zhang, H. Yu, T. Li, *et al.*, Hierarchical trimetallic layered double hydroxide nanosheets derived from 2D metal-organic frameworks for enhanced oxygen evolution reaction, *Appl. Catal. B*, 264(2020), art. No. 118532.

[13] L. Reith, J.N. Hausmann, S. Mebs, *et al.*, *In situ* detection of iron in oxidation states ≥ IV in cobalt–iron oxyhydroxide reconstructed during oxygen evolution reaction, *Adv. Energy Mater.*, 13(2023), No. 12, art. No. 2203886.

[14] M. Batool, A. Hameed, and M.A. Nadeem, Recent developments on iron and nickel-based transition metal nitrides for overall water splitting: A critical review, *Coord. Chem. Rev.*, 480(2023), art. No. 215029.

[15] S. Ghosh, B. Dasgupta, S. Kalra, *et al.*, Evolution of carbonate-intercalated γ-NiOOH from a molecularly derived nickel sulfide (pre)catalyst for efficient water and selective organic oxidation, *Small*, 19(2023), No. 16, art. No. 2206679.

[16] Z.Y. Yu, Y. Duan, J.D. Liu, *et al.*, Unconventional CN vacancies suppress iron-leaching in Prussian blue analogue pre-catalyst for boosted oxygen evolution catalysis, *Nat. Commun.*, 10(2019), art. No. 2799.

[17] Z.Y. Yu, Y. Duan, X.Y. Feng, X.X. Yu, M.R. Gao, and S.H. Yu, Clean and affordable hydrogen fuel from alkaline water

splitting: Past, recent progress, and future prospects, *Adv. Mater.*, 33(2021), No. 31, art. No. 2007100.

[18] T.Z. Wu, S.N. Sun, J.J. Song, *et al.*, Iron-facilitated dynamic active-site generation on spinel $CoAl_2O_4$ with self-termination of surface reconstruction for water oxidation, *Nat. Catal.*, 2(2019), No. 9, p. 763.

[19] Y.M. Sun, X. Ren, S.N. Sun, Z. Liu, S.B. Xi, and Z.J. Xu, Engineering high-spin state cobalt cations in spinel zinc cobalt oxide for spin channel propagation and active site enhancement in water oxidation, *Angew. Chem. Int. Ed.*, 60(2021), No. 26, p. 14536.

[20] F. Yu, H.Q. Zhou, Y.F. Huang, *et al.*, High-performance bifunctional porous non-noble metal phosphide catalyst for overall water splitting, *Nat. Commun.*, 9(2018), art. No. 2551.

[21] J.J. Gao, H.B. Tao, and B. Liu, Progress of nonprecious-metal-based electrocatalysts for oxygen evolution in acidic media, *Adv. Mater.*, 33(2021), No. 31, art. No. 2003786.

[22] X.J. Li, H.K. Zhang, Q. Hu, *et al.*, Amorphous NiFe oxide-based nanoreactors for efficient electrocatalytic water oxidation, *Angew. Chem. Int. Ed.*, 62(2023), No. 15, art. No. e202300478.

[23] Q.W. Zhang, Y.X. Hu, H.F. Wu, *et al.*, Entropy-stabilized multicomponent porous spinel nanowires of $NiFeXO_4$ (X = Fe, Ni, Al, Mo, Co, Cr) for efficient and durable electrocatalytic oxygen evolution reaction in alkaline medium, *ACS Nano*, 17(2023), No. 2, p. 1485.

[24] J.F. Zhang, Y. Jiang, Y. Wang, *et al.*, Ultrathin carbon coated mesoporous Ni–$NiFe_2O_4$ nanosheet arrays for efficient overall water splitting, *Electrochim. Acta*, 321(2019), art. No. 134652.

[25] X.K. Chen, X.H. Zhang, L.Z. Zhuang, *et al.*, Multiple vacancies on (111) facets of single-crystal $NiFe_2O_4$ spinel boost electrocatalytic oxygen evolution reaction, *Chem. Asian. J.*, 15(2020), No. 23, p. 3995.

[26] H.W. Xu, B. Liu, J.Y. Liu, Y. Yao, Z.G. Gu, and X.D. Yan, Revealing the surface structure-performance relationship of interface-engineered NiFe alloys for oxygen evolution reaction, *J. Colloid Interface Sci.*, 622(2022), p. 986.

[27] M. Zhao, H.L. Li, W.Y. Yuan, and C.M. Li, Tannic acid-mediated *in situ* controlled assembly of NiFe alloy nanoparticles on pristine graphene as a superior oxygen evolution catalyst, *ACS Appl. Energy Mater.*, 3(2020), No. 4, p. 3966.

[28] Q.L. Kang, D.W. Lai, W.Y. Tang, Q.Y. Lu, and F. Gao, Intrinsic activity modulation and structural design of NiFe alloy catalysts for an efficient oxygen evolution reaction, *Chem. Sci.*, 12(2021), No. 11, p. 3818.

[29] F.L. Zhou, M.X. Gan, D.F. Yan, X.L. Chen, and X. Peng, Hydrogen-rich pyrolysis from Ni–Fe heterometallic Schiff base centrosymmetric cluster facilitates NiFe alloy for efficient OER electrocatalysts, *Small*, 19(2023), No. 24, art. No. 2208276.

[30] X. Shi, A.P. Wu, H.J. Yan, *et al.*, A "MOFs plus MOFs" strategy toward Co–Mo_2N tubes for efficient electrocatalytic overall water splitting, *J. Mater. Chem. A*, 6(2018), No. 41, p. 20100.

[31] C.S. Cao, D.D. Ma, Q. Xu, X.T. Wu, and Q.L. Zhu, Semisacrificial template growth of self-supporting MOF nanocomposite electrode for efficient electrocatalytic water oxidation, *Adv. Funct. Mater.*, 29(2019), No. 6, art. No. 1807418.

[32] K. Ge, S.J. Sun, Y. Zhao, *et al.*, Facile synthesis of two-dimensional iron/cobalt metal-organic framework for efficient oxygen evolution electrocatalysis, *Angew. Chem. Int. Ed.*, 60(2021), No. 21, p. 12097.

[33] J.P. Hu, Y.Z. Qin, H. Sun, *et al.*, Combining multivariate electrospinning with surface MOF functionalization to construct tunable active sites toward trifunctional electrocatalysis, *Small*, 18(2022), No. 9, art. No. 2106260.

[34] F.L. Li, Q. Shao, X.Q. Huang, and J.P. Lang, Nanoscale trimetallic metal-organic frameworks enable efficient oxygen evolution electrocatalysis, *Angew. Chem. Int. Ed.*, 57(2018), No. 7, p. 1888.

[35] X. Zhang, J.S. Luo, K. Wan, *et al.*, From rational design of a new bimetallic MOF family with tunable linkers to OER catalysts, *J. Mater. Chem. A*, 7(2019), No. 4, p. 1616.

[36] D.K. Wang, M.J. Suo, S.Q. Lai, *et al.*, Photoinduced acceleration of Fe^{3+}/Fe^{2+} cycle in heterogeneous FeNi-MOFs to boost peroxodisulfate activation for organic pollutant degradation, *Appl. Catal. B*, 321(2023), art. No. 122054.

[37] V.H. Nguyen, T.D. Nguyen, L.G. Bach, *et al.*, Effective photocatalytic activity of mixed Ni/Fe-base metal-organic framework under a compact fluorescent daylight lamp, *Catalysts*, 8(2018), No. 11, art. No. 487.

[38] Z.D. Huang, J.H. Liu, Z.Y. Xiao, *et al.*, A MOF-derived coral-like NiSe@NC nanohybrid: An efficient electrocatalyst for the hydrogen evolution reaction at all pH values, *Nanoscale*, 10(2018), No. 48, p. 22758.

[39] D. Chen, J.W. Zhu, X.Q. Mu, *et al.*, Nitrogen-doped carbon coupled $FeNi_3$ intermetallic compound as advanced bifunctional electrocatalyst for OER, ORR and Zn-air batteries, *Appl. Catal. B*, 268(2020), art. No. 118729.

[40] K. Ji, Y.L. Yue, and P. Yang, Interface effect in MIL-53(Fe)/metal-phenolic network (Ni, Co, and Mn) nanoarchitectures for efficient oxygen evolution reaction, *Appl. Surf. Sci.*, 608(2023), art. No. 155184.

[41] X. Meng, J.H. Xie, Y.B. Sun, *et al.*, Fe_2O_3/spinel $NiFe_2O_4$ heterojunctions *in-situ* wrapped by one-dimensional porous carbon nanofibers for boosting oxygen evolution/reduction reactions, *Int. J. Hydrogen Energy*, 47(2022), No. 50, p. 21329.

[42] W.J. Gong, H.Y. Zhang, L. Yang, Y. Yang, J.S. Wang, and H. Liang, Core@shell MOFs derived Co_2P/CoP@NPGC as a highly-active bifunctional electrocatalyst for ORR/OER, *J. Ind. Eng. Chem.*, 106(2022), p. 492.

[43] S. Seok, M. Choi, Y. Lee, *et al.*, Ni nanoparticles on Ni core/N-doped carbon shell heterostructures for electrocatalytic oxygen evolution, *ACS Appl. Nano Mater.*, 4(2021), No. 9, p. 9418.

[44] D.D. Qi, X. Chen, W.P. Liu, *et al.*, A Ni/Fe-based heterometallic phthalocyanine conjugated polymer for the oxygen evolution reaction, *Inorg. Chem. Front.*, 7(2020), No. 3, p. 642.

[45] Y.Y. Guo, Q. Huang, J.Y. Ding, *et al.*, CoMo carbide/nitride from bimetallic MOF precursors for enhanced OER performance, *Int. J. Hydrogen Energy*, 46(2021), No. 43, p. 22268.

[46] S.F. Tan, W.M. Ouyang, Y.J. Ji, and Q.W. Hong, Carbon wrapped bimetallic NiCo nanospheres toward excellent HER and OER performance, *J. Alloys Compd.*, 889(2021), art. No. 161528.

[47] Y.C. Zheng, G.K. Zhang, P.J. Zhang, *et al.*, Structural investigation of metallic Ni nanoparticles with N-doped carbon for efficient oxygen evolution reaction, *Chem. Eng. J.*, 429(2022), art. No. 132122.

[48] J. Lu, S. Ji, P. Kannan, H. Wang, X.Y. Wang and R.F. Wang, Hydrophilic $Ni(OH)_2$@CoB nano-chains with shell-core structure as an efficient catalyst for oxygen evolution reaction, *J. Alloys Compd.*, 844(2020), art. No. 156129.

[49] S.H. Park, S.H. Kang, and D.H. Youn, Direct one-step growth of bimetallic Ni_2Mo_3N on Ni foam as an efficient oxygen evolution electrocatalyst, *Materials*, 14(2021), No. 16, art. No. 4768.

[50] G. Yuan, Y.J. Hu, Z.H. Wang, *et al.*, Facile synthesis of self-supported amorphous phosphorus-doped $Ni(OH)_2$ composite anodes for efficient water oxidation, *Catal. Sci. Technol.*, 10(2020), No. 1, p. 263.

[51] H.M.A. Amin, M. Attia, D. Tetzlaff, and U.P. Apfel, Tailoring the electrocatalytic activity of pentlandite $Fe_xNi_{9-x}S_8$ nanoparticles via variation of the Fe : Ni ratio for enhanced water oxidation, *ChemElectroChem*, 8(2021), No. 20, p. 3863.

[52] Z.Y. Chen, X.L. Liu, T. Shen, C.Z. Wu, L.G. Zu, and L. Zhang, Porous NiFe alloys synthesized via freeze casting as bifunctional electrocatalysts for oxygen and hydrogen evolution reaction, *Int. J. Hydrogen Energy*, 46(2021), No. 76, p. 37736.